1 *Title page*

2 **ROCK inhibitor enhances mitochondrial transfer via tunneling nanotubes in**
3 **retinal pigment epithelium**

4

5 Jing Yuan[1], Fangxuan Chen[2], Dan Jiang[3], Zehua Xu[1], Hang Zhang[1], Zi-Bing Jin[1, *]

6

7 [1]Beijing Institute of Ophthalmology, Beijing Tongren Eye Center, Beijing Tongren
8 Hospital, Capital Medical University, Beijing, 100730, China;
9 [2]Clinical Pathology Diagnostic Center, Ningbo, Zhejiang, 315020, China;
10 [3]National Clinical Research Center for Ocular Diseases, Eye Hospital, Wenzhou
11 Medical University, Wenzhou, 325027, China.
12 [*]**Correspondence:** Profs. Zi-Bing Jin, Beijing Institute of Ophthalmology, Beijing
13 Tongren Hospital, Capital Medical University, Beijing, 100730, China.
14 **E-mail:** jinzb502@ccmu.edu.cn

15

16 **Abstract**
17 **Rationale:** Tunnel nanotube (TNT)-mediated mitochondrial transport is crucial for
18 the development and maintenance of multicellular organisms. Despite numerous
19 studies highlighting the significance of this process in both physiological and
20 pathological contexts, knowledge of the underlying mechanisms is still limited. This
21 research focused on the role of the ROCK inhibitor Y-27632 in modulating TNT
22 formation and mitochondrial transport in retinal pigment epithelial (RPE) cells.
23 **Methods:** Two types of ARPE19 cells (a retinal pigment epithelial cell line) with
24 distinct mitochondrial fluorescently labeled, were co-cultured and treated with ROCK
25 inhibitor Y-27632. The formation of nanotubes and transport of mitochondria were
26 assessed through cytoskeletal staining and live cell imaging. Mitochondrial
27 dysfunction was induced by light damage to establish a model, while mitochondrial
28 function was evaluated through measurement of oxygen consumption rate. The effects
29 of Y-27632 on cytoskeletal and mitochondrial dynamics were further elucidated
30 through detailed analysis.
31 **Results:** Y-27632 treatment led to an increase in nanotube formation and enhanced
32 mitochondrial transfer among ARPE19 cells, even following exposure to
33 light-induced damage. Our analysis of cytoskeletal and mitochondrial distribution
34 changes suggests that Y-27632 promotes nanotube-mediated mitochondrial transport
35 by influencing cytoskeletal remodeling and mitochondrial movement.
36 **Conclusions**: These results suggest that Y-27632 has the ability to enhance
37 mitochondrial transfer via tunneling nanotubes in retinal pigment epithelium, and
38 similarly predict that ROCK inhibitor can fulfill its therapeutic potential through
39 promoting mitochondrial transport in the retinal pigment epithelium in the future.

40

Graphical abstract
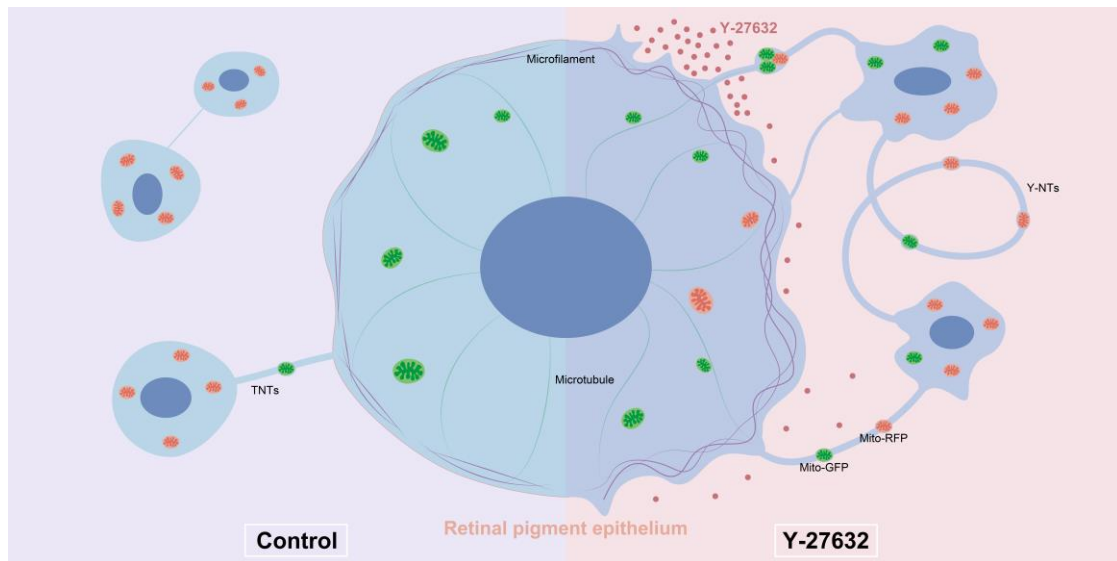
Background

Material exchange between cells is crucial for the maintenance and development of multicellular organisms[1-4], and intercellular mitochondrial transport serves as a prime example of such material exchange[1, 5-8]. Mitochondria, as vital organelles in eukaryotic cells, play a key role in providing cellular energy[9, 10]. Previous research has confirmed that mitochondrial transfer between cells is a common occurrence. Under physiological conditions, mitochondrial transfer is associated with tissue development and dynamic balance of energy[11]. In pathological conditions, mitochondrial dysfunction triggers more active mitochondrial transfer to replenish damaged cells with exogenous healthy mitochondria, aiming to restore cellular energy and facilitate disease regression[12, 13]. The transfer of mitochondria from donor to recipient cells appears to be a potential therapeutic modality for rescuing diseased cells[14-16].

Among the mitochondrial transfer pathways reported to date, tunneling nanotubes (TNTs) are recognized as the principal cytoarchitecture for mitochondrial transportation[17]. The pioneering work by Rustom et al. in 2004 initially highlighted the role of TNTs in facilitating the transport of vesicles and organelles[18]. Subsequently, Spees et al. in 2006 demonstrated the transfer of functional mitochondria from mesenchymal stem cells (MSCs) to dysfunctional mammalian cells, thereby restoring aerobic respiration[19]. TNTs can be formed by the extension of filamentous pseudopods into neighboring cells or by separating two contacting cells[20, 21]. Structurally, TNTs are defined by their abundance of F-actin, suspension in the culture medium, and lack of attachment to the extracellular substrate[22, 23]. Functionally, TNTs exhibit the capacity to transport proteins, vesicles, organelles, RNA, and pathogens between nonadjacent cells[23-25]. Serving as a novel long-distance intercellular communication pathway, TNTs not only facilitate the

73   exchange of intercellular cargoes and organelles but also contribute to intracellular
74   homeostasis by balancing intercellular stress through material exchange[26]. However,
75   the underlying molecular mechanisms governing TNT formation, particularly the
76   endogenous mechanisms, remain elusive.
77   Currently known methods that can regulate TNT-mediated mitochondrial
78   transport include two aspects: one is increasing the chance of mitochondrial transport
79   occurring by increasing the demand for mitochondrial energy synthesis of recipient
80   cell[27-30]; another is increasing the number of mitochondria transport by enhancing
81   the expression of relevant transporter proteins in the donor cell[31]. The cytoskeleton
82   is a major component of TNT, and mitochondrial transport within the cell is to some
83   extent dependent on the cytoskeleton. Here, we propose a new conjecture that TNT is
84   essentially a specialized filamentous protrusion, so could TNT formation be increased
85   by altering the arrangement of the cytoskeleton thereby further increasing the chances
86   of mitochondrial transfer between cells?
87   Rho GTPases play a crucial role in regulating cytoskeleton dynamics, with key
88   members including RhoA, Rac1, and CDC42. The downstream protein of RhoA,
89   ROCK, can be inhibited by Y-27632[32, 33]. Our previous research has demonstrated
90   the transfer of mitochondria between mesenchymal stem cells (MSCs) and different
91   types of ocular cells through tunneling nanotubes based on F-actin[1]. Additionally,
92   studies by Robin Ali have shown that mammalian photoreceptor neurons can form
93   open nanotube-like protrusions and mediate mitochondrial transfer[34]. In this study,
94   we focused on the retinal pigment epithelium (RPE) to investigate the effect of the
95   ROCK inhibitor Y-27632 on the pattern of mitochondrial transfer between
96   homologous cells, as well as exploring the potential benefits of enhanced
97   mitochondrial transport on self-repair in cells with dysfunctional mitochondria. We
98   look forward to bringing new insights into intercellular mitochondrial transfer
99   mechanisms.
100
101   **Results**
102
103   **Y-27632 enhanced intercellular nanotube formation and mitochondrial transfer**
104
105   Previous studies have shown that actin polymerization is essential for the
106   formation of TNT, with the RhoGTPase family, particularly ROCK, playing a
107   regulatory role in the actin cytoskeleton[35, 36]. Y-27632, a specific inhibitor of the
108   ROCK pathway, has been reported to promote axon extension in nerve injury[37].
109   Therefore, we investigated the potential of Y-27632 in modulating TNT formation.
110   Here, we investigated the potential of Y-27632 treated ARPE19 cells to form
111   intercellular nanotubes, and the exchange of organelles, specifically mitochondria,
112   between ARPE19 cells through this mechanism. Thin, membranous structures
113   connecting two cells were observed following the addition of 10µM Y-27632 to the
114   culture medium (Figure 1A). Intercellular transfer of mitochondria was assessed using

mito-GFP labeled ARPE19 cells as donor cells and ARPE19 cells stained with cell trace violet (cytoplasmic membrane, CM) as recipient cells. The two types of cells were co-cultured at a 1:1 ratio (Figure 1B). Nanotube formation and mitochondrial transport between ARPE19 cells were visualized using confocal microscopy followed by treatment with varying concentrations of Y-27632 for 24 hours (Figure 1C). Phalloidin staining demonstrated a significant increase in Y-27632-induced nanotube formation with escalating concentrations of Y-27632, especially when it was increased to 40μM (Figure 1D). Moreover, a notable enhancement in mitochondrial transfer rate was observed with increasing Y-27632 concentration, suggesting a potential role for Y-27632 in facilitating nanotube-mediated mitochondrial transfer between ARPE19 cells (Figure 1E). In order to confirm the role of ROCK inhibitors in promoting nanotube formation and mitochondrial transfer, we further investigated the effects of the ROCK inhibitors Y-39983 and GSK269962A on nanotube formation and mitochondrial transfer in ARPE19 cells. The findings revealed that treatment with 10μM of Y-39983 and 10μM of GSK269962A also resulted in a significant enhancement of both nanotube formation and mitochondrial transfer in ARPE19 cells (Figure S1A, B and C). Subsequently, the impact of escalating Y-27632 concentrations on ARPE19 cells was evaluated. Quantitative analysis of Annexin V and PI assays revealed a decrease in cell viability and an increase in apoptosis rates in ARPE19 cells treated with concentrations exceeding 40μM (Figure 1F, G, H, and I). Therefore, 40μM of Y-27632 treatment was selected for inducing nanotube formation and mitochondrial transfer in subsequent experiments.

Characterization of Y-27632-induced intercellular nanotubes

To further investigate mitochondrial exchange, stable ARPE19-mito-GFP and ARPE19-mito-RFP cell lines were generated, wherein mitochondria were labeled with mito-GFP and mito-RFP, respectively (Figure S2A and B). Co-culturing ARPE19-mito-GFP cells with ARPE19-mito-RFP cells stained with cytoplasmic membrane (CM) at a 1:1 ratio for 24 hours revealed the presence of GFP-labeled mitochondria derived from donor cells in CM$^+$ recipient cells (Figure 2A and B). Additionally, Y-27632 treatment was found to enhance nanotube formation and mitochondrial transfer (Figure S3A and B). The capacity of cells to both receive mitochondria from other cells (transfer in) and transfer their mitochondria to other cells (transfer out) was quantified following Y-27632 treatment. Cells in a normal state have no significant difference in the ability of mitochondria to transfer in and out, whether or not enhanced by using Y-27632 (Figure 2C). To investigate the role of Y-27632-induced nanotube in mitochondrial transfer, we utilized a co-culture test that was previously documented[1]. In this experimental setup, ARPE19 cells labeled with mito-GFP were designated as the donor cells, co-culturing with unlabeled recipient ARPE19 cells in a transwell with a 0.4μm pore size filter separating the two cell populations (Figure 2D). Recipient cells that received mitochondria from donors were

157 examined using confocal microscopy after being co-cultured for 24 hours. Cell-cell
158 contact was necessary for the observed transfer of mitochondria, as the transfer was
159 nearly undetectable when recipient and donor cells were cultured separately in a
160 transwell with a filter barrier (Figure 2E). F-actin typically serves as a crucial
161 constituent of tunneling nanotubes (TNTs), with the presence of tubulin also noted in
162 specific cell types exhibiting thicker TNTs. Some studies have indicated that TNTs
163 between ARPE19 cells exclusively consist of F-actin[38]. Consequently, we
164 investigated the composition of Y-27632-induced nanotubes (Figure 2F). Our findings
165 revealed that the majority (83.33%) of nanotubes between untreated ARPE19 cells
166 comprised solely F-actin. However, approximately 64.22% of Y-27632-induced
167 nanotubes contained both F-actin and tubulin (Figure 2G). It is plausible that TNTs
168 containing microtubules may facilitate mitochondrial transport due to their larger
169 diameter.

170   Intercellular nanotubes exhibit a wide range of lengths, varying from a few to
171 over a hundred micrometers, and may display curvature and branching, as evidenced
172 in ARPE19 cells (Figure 2I, Figure S2C). The length of nanotubes in both control and
173 Y-27632 treated groups was quantified. Y-27632-induced nanotubes demonstrated a
174 significantly greater average length (30.00±27.28µm) compared to nanotubes in the
175 control group (12.48±11.04µm) (Figure 2H). Given the characteristic feature of TNTs
176 being non-adherent to the extracellular substrate, we conducted z-axis imaging to
177 examine these membranous structures. Staining of the cytoplasmic membrane (CM)
178 revealed that these structures were indeed adherent to the extracellular substrate
179 (Figure 2J). The Y-27632-induced nanotubes appear distinct from conventional TNTs,
180 hence termed as Y-NTs. Scanning electron microscope (SEM) images depict various
181 types of Y-NTs (Figure 2K).

182   To validate the functionality of Y-NTs in ARPE19 cells for transporting cargoes
183 like mitochondria between interconnected cells, we conducted a live cell imaging
184 assay using ARPE19-mito-GFP cells and CM$^+$ ARPE19 cells. Through time-lapse
185 confocal microscopy (see Movie 1, 2, and 3), we observed the formation of Y-NTs
186 (Figure 2L1), the entry of mitochondria into recipient cells (Figure 2L2), and the
187 movement of mitochondria along Y-NTs (Figure 2L3). These findings provide
188 evidence that Y-NTs facilitate mitochondrial transfer between ARPE19 cells.

189

190 **Cytoskeletal inhibition eliminates Y-NTs-mediated mitochondrial transfer**

191

192   The interaction between mitochondria and the cytoskeleton is essential for the
193 proper functioning of mitochondria[39]. Previous studies have indicated that the
194 movement of mitochondria over long distances is facilitated by microtubules, whereas
195 short-term movement is mediated by actin filaments[40]. To investigate whether the
196 increase of mitochondrial transfer in Y-27632 treated cells depends on the actin
197 filaments or microtubules, we utilized Cytochalasin B (Cyto B) and Nocodazole
198 (Noco), which are known to depolymerize F-actin and microtubules, respectively.

199 After treating with either Cyto B or Noco, in addition to vehicle control (DMSO), the
200 formation of Y-NTs and mitochondrial transfer were assessed using confocal
201 microscopy (Figure 3A). In Y-27632 treated cells, depolymerization of F-actin
202 inhibited the formation of nanotubes and the transfer of mitochondria. Similarly,
203 treatment with Nocodazole reduced mitochondrial transport, yet did not completely
204 abolish the stimulatory effect of Y-27632 on nanotube formation (Figure 3B and C).
205 Our findings demonstrate that the formation of Y-NTs is predominantly reliant on
206 actin filaments, while the transport of mitochondria may depend on microtubules for
207 Y-27632-induced long-distance movement.
208
209 **Y-NTs mediated mitochondrial transfer rescues light-damaged ARPE19 cells**
210
211 Functional mitochondrial transfer has the potential to rescue cells with
212 mitochondrial dysfunction, which always requires MSC involvement[27-30]. Our
213 study aimed to investigate the impact of Y-27632 on enhancing the self-repair
214 capacity of ARPE19 cells through modulation of mitochondrial transport via Y-NTs.
215 To assess the efficacy of this modulation, we conducted experiments using a
216 co-culture assay and subjected the cells to light damage (LD) to evaluate their
217 survival rates.
218 To validate our findings, we developed a light damage model of mitochondrial
219 dysfunction[41]. ARPE19 cells were initially exposed to varying durations of blue
220 light (19klux, 330-340nm) to induce light damage. Flow cytometry analysis was used
221 to quantify mitochondrial dysfunction by labeling JC-1 in different experimental
222 groups (Figure 4A). A 2-hour exposure duration was selected for subsequent
223 experiments, during which a 23.7% decrease in mitochondrial membrane potential
224 was observed (Figure 4B). Hoechst 33342 staining also revealed light-induced
225 apoptosis (Figure 4C). Additionally, light-induced mitochondrial dysfunction was
226 assessed using the XF cell mito stress test (Figure 4D), which showed significant
227 reductions in both basal and maximal respiratory capacity, ATP production and spare
228 respiratory capacity following light damage (Figure 4E).
229 Subsequently, alterations in mitochondrial transfer patterns were evaluated. The
230 experiments were conducted following the programs in Figure 4F. Co-cultures were
231 established between CM+ ARPE19-mito-RFP cells, with or without light-induced
232 damage, and healthy ARPE19-mito-GFP cells at a 1:1 ratio, in the absence or
233 presence of Y-27632 (Figure 4F). The transfer of mito-GFP labeled mitochondria
234 from ARPE19-mito-GFP to ARPE19-mito-RFP cells was visualized as punctate green
235 or yellow regions in CM+ light-damaged cells (Figure 4G). Light damage did not
236 augment mitochondrial transfer in ARPE19 cells; however, Y-27632 treatment
237 potentiated mitochondrial transfer under both normal and light damage conditions.
238 Furthermore, light-damaged ARPE19 cells exhibited a significantly higher propensity
239 for mitochondrial transfer inward compared to outward transfer (Figure 4H). These
240 findings indicate that Y-27632 modulates mitochondrial transfer patterns in cells with

241 mitochondrial dysfunction.

242   Following light-induced damage, CM$^+$ ARPE19 cells were subsequently cultured
243 or co-cultured with healthy ARPE19 cells at a 1:1 ratio in the presence or absence of
244 Y-27632. After a 24-hour incubation period, mitochondrial function was assessed
245 using seahorse analysis (Figure 4I). Co-cultivation with healthy cells resulted in a
246 significant reversal of the energy metabolism impairment observed in light-damaged
247 cells compared to monocultured cells (Figure 4J, Figure S4A), as evidenced by
248 increased basal respiration, maximal respiration, and spare respiration capacity
249 (Figure S4B). Unfortunately, treatment with Y-27632 did not yield a discernible
250 difference in co-cultured cells compared to untreated co-cultured cells.

251

252 **Y-27632 regulates cytoskeleton remodeling**

253

254   Previous research has shown that the Rho GTPase family plays a role in
255 regulating the cytoskeleton, specifically F-actin. It has been documented that F-actin
256 dynamics are crucial for the formation of TNTs[35, 36, 42]. Therefore, we
257 investigated the impact of Y-27632 on F-actin polymerization in ARPE19 cells. Live
258 cell imaging (see Movie 2) revealed significant changes in cytoskeletal organization
259 and cell movement upon Y-27632 treatment compared to untreated cells, with
260 ARPE19 cells extending axon-like structures to establish connections with
261 neighboring cells (Figure 5A). Furthermore, the average cell attachment area
262 increased from 1307±619.4μm² to 2089±827.3μm², and the cell outline length
263 expanded from 150.5±43.74μm to 264.0±83.74μm following Y-27632 treatment
264 (Figure 5B and C). To examine the intricate structure of cell morphology, the cells
265 were analyzed using scanning electron microscopy and super-resolution confocal
266 microscopy. Normal ARPE19 cells exhibited prominently raised cytosol and tightly
267 organized cytosolic actin filaments. Upon treatment with Y-27632, the cells displayed
268 a more malleable and pliable nature, facilitating the formation of various structures
269 such as filamentous pseudopods, platelike feet, and inter-cellular connections.
270 Additionally, the distribution of microfilaments throughout the entire cell was more
271 uniform and consistent (Figure 5D and E). These findings suggest an increased
272 likelihood of intercellular nanotube formation compared to control cells, which
273 exhibited minimal changes in cell morphology (see Movie 4).

274   Subsequent investigation delved into the impact of Y-27632 on cytoskeletal
275 alterations at the molecular protein level. RNA sequencing analysis unveiled a
276 tendency towards differential expression in certain cytoskeletal molecules, albeit
277 lacking statistical significance (Figure 5F). Protein expression of F-actin and tubulin
278 similarly exhibited no significant alterations (Figure 5G). These findings suggest that
279 treatment with 40μM Y-27632 induced cytoskeletal reorganization without eliciting
280 notable changes in the expression of key skeletal proteins.

281

282 **Y-27632 promotes mitochondrial movement in response to cytoskeletal changes**

283

Subcellular distribution of mitochondria was assessed to determine the impact of Y-27632. Mitochondria were classified based on established subcellular distribution patterns[43], and quantitative analysis was conducted in control and Y-27632 groups. Similar to the published study[43], we identified three categories of mitochondrial arrangement: polarized (grouped around one side of the nucleus), perinuclear (spread around the nucleus), and infiltrating (entering the cortical cytoskeleton). Additionally, a novel mitochondrial distribution pattern termed axon-like (forming bundles resembling axons) was observed in the Y-27632 group that could not be categorized into the three previously mentioned (Figure 6A). Control cells predominantly exhibited a "polarized" and "perinuclear" pattern, while Y-27632 treated cells displayed elongated mitochondria with an "infiltrating" and "axon-like" pattern. The percentage of "polarized" and "perinuclear" mitochondria decreased from 52.34% and 26.17% to 7.22% and 6.19%, respectively, while "infiltrating" and "axon-like" mitochondria increased from 18.69% and 2.80% to 49.48% and 37.11%, respectively (Figure 6B).

In the live cell imaging assay conducted (see Movie 3), it was observed that mitochondria exhibited a tendency to cluster around the nucleus and displayed minimal movement in control cells. Conversely, in cells treated with Y-27632, a significant portion of mitochondria demonstrated heightened mobility and penetrated into the cortical cytoskeleton, aligning with cytoskeletal dynamics (Figure 6C, Movie 2). The movement of mitochondria was found to be mediated by the miro1 protein, which governs mitochondrial transport along microtubules by facilitating the connection between mitochondria and motor proteins[39, 44]. Notably, treatment with Y-27632 was shown to impact mitochondrial dynamics by upregulating the expression of miro1 (Figure 6D, Figure S5A, and B). As a member of the GTPase family and localized on the outer mitochondrial membrane, miro1 plays a pivotal role in regulating mitochondrial transport and distribution[45]. Recent studies have highlighted the ability of the miro1 protein to coordinate mitochondrial movement and positioning through interactions with actin and microtubules[46].

To further analyze the impact of Y-27632 on mitochondria, we conducted mitochondrial network structure analysis using ImageJ software (Figure 6E). Quantitative assessment revealed an increased number of individual mitochondria in cells treated with Y-27632 (Figure 6F). Moreover, the average length of individual mitochondria in Y-27632-treated cells was significantly greater compared to untreated cells (Figure 6G). The network number and size of mitochondria showed no significant differences with Y-27632 treatment (Figure S4D and E). These findings suggest that Y-27632 maintains mitochondria in a metabolically active and readily transportable state, facilitating their infiltration into the cortical cytoskeleton.

Discussion

325　　　Over the nearly two decades since their discovery, tunneling nanotubes (TNTs)
326　have been acknowledged as an additional mechanism for intercellular communication,
327　facilitating the exchange of various cellular cargo among cells, and they have shown
328　significant potential in various diseases and pathological processes [21, 23]. Despite
329　the identification of TNTs and TNT-like structures in diverse cell types cultured in
330　vitro, such as immune cells, kidney cells, epithelial cells, tumor cells, neurons,
331　astrocytes, and retinal cells, there is a substantial gap in understanding the molecular
332　mechanisms governing the formation and functionality of these enigmatic
333　structures[47]. The outward polymerization, targeted regulation, and local
334　deformation of the plasma membrane of F-actin all promote the outward extension of
335　TNT[23].

336　　　In this study, we observed that the ROCK inhibitor Y-27632 stimulates an
337　increase in nanotube-mediated mitochondrial transfer among retinal pigment
338　epithelial cells. In addition to Y-27632, the ROCK inhibitors Y-39983 and
339　GSK269962A also elicited similar effects on ARPE19 cells. Several studies in other
340　cells on the promotion of mitochondrial transfer by ROCK inhibitors similarly
341　support the present study[42, 48, 49]. However, our findings first indicate that
342　Y-27632 induces alterations in cell morphology by regulating the organization of
343　cytoskeletal elements, specifically actin filaments and microtubules, leading to the
344　formation of protrusion-like structures that extend into neighboring cells, thereby
345　promoting nanotube formation. These nanotubes, enriched with microtubule
346　structures, facilitate frequent mitochondrial transport. Furthermore, Y-27632 promotes
347　the intracellular movement of mitochondria from perinuclear clusters to a dispersed
348　distribution within the cellular cytoskeleton, accompanied by the extension of cellular
349　protrusions, which in turn enhances transcellular mitochondrial transport. Disruption
350　of actin filaments and microtubules abolishes the facilitating effect of Y-27632.
351　Notably, light-damaged recipient ARPE19 cells treated with Y-27632 exhibit
352　increased mitochondrial respiration following the uptake of more mitochondria from
353　healthy ARPE19 cells. These results suggest that the promotion of mitochondrial
354　transfer between homologous cells can be achieved by pharmacological intervention
355　to enhance cellular self-repair mechanisms, rather than relying on exogenous
356　mitochondrial donor cells.

357　　　Our findings suggest that mitochondrial intercellular transfer is a natural
358　physiological process in retinal pigment epithelium (RPE) cells, and treatment with
359　Y-27632 (40μM) promotes an increase in the formation of RPE intercellular
360　nanotubes (Y-NTs) and enhances the rate of mitochondrial transfer. Compared to
361　regular TNTs, Y-NTs exhibit longer average lengths, leading to a higher presence of
362　microtubules alongside F-actin and attachment to extracellular substrates. These
363　characteristics contribute to a more robust structure, increased resistance to
364　mechanical damage, and facilitate longer-distance material transport. The
365　development of Y-NTs relies heavily on actin filaments and microtubules, with
366　mitochondrial transport being predominantly microtubule-dependent. Inhibition of

actin filament and microtubule aggregation abolishes the Y-27632-induced increase in nanotubules and mitochondrial transfer. Disruption of actin filaments alone results in a reduction in Y-NT formation and mitochondrial transfer, while disruption of microtubules alone decreases mitochondrial transfer without affecting the number of TNTs. These findings suggest that Y-NT formation primarily hinges on actin filaments, whereas Y-27632-induced mitochondrial transfer is predominantly reliant on microtubules.

Mitochondria serve as the primary cargo transported through tunneling nanotubes (TNTs), with TNT-mediated mitochondrial transfer potentially affecting cell survival and adaptation[47]. For instance, the transfer of mitochondria via TNTs in healthy cells has been shown to rescue cell apoptosis triggered by UV exposure[50]. In this investigation, we assessed the efficacy of mitochondrial transfer in both inbound and outbound directions. In Y-27632-treated light-damaged retinal pigment epithelial (RPE) cells, the capacity for inbound mitochondrial transfer was found to be more robust than outbound transfer. Our findings also indicate that Y-27632 treatment enhances the ability of healthy cells to rescue light-damaged cells in our co-culture system, particularly by augmenting basal and maximal respiratory capacity.

In the human eye, the retinal pigment epithelial cells form a tight connection, establishing the outer retinal barrier[51]. ARPE19, a cell line of retinal pigment epithelial cells, exhibits a stable and well-defined cellular morphology, characterized by the orderly arrangement of actin filaments at the cell membrane and limited cell motility, thereby minimizing long-range interactions with neighboring cells. Our observations using live cell imaging revealed that treatment with Y-27632 induced notable alterations in the cytoskeletal organization of ARPE19 cells, including an increase in cell adhesion area, enhanced cellular contour, reduced density of actin filaments at the membrane, heightened cellular plasticity, a tendency towards extending dendritic structures for intercellular contact, and augmented cell motility. These cellular modifications induced by Y-27632 likely promote the formation of nanotubes among RPE cells.

Y-27632 has been shown to modify the subcellular localization of mitochondria, leading to their enhanced penetration into the cortical cytoskeleton. Additionally, Y-27632 induces the extension of mitochondria with dendritic-like structures, resembling mitochondrial axonal transport in neuronal cells. It has been suggested that inhibition of PI3K could result in the redistribution of energetically active mitochondria to the cortical cytoskeleton, thereby promoting the motility and invasion of tumor cells. This redistribution alters mitochondrial membrane dynamics and enhances random cell motility[43]. Studies have indicated that localized activation of energy sensors and the metabolic regulator AMPK can stimulate forward migration of mitochondria, maintain ATP content, and ensure the ATP supply required for cell migration[52]. These findings suggest that the redistribution of mitochondrial membranes induced by Y-27632 is a response to the energy requirements associated with changes in cytoskeletal structure, potentially facilitating mitochondrial transport

409   across cells.
410   Mitochondria are highly active organelles that play a crucial role in facilitating
411   exchange by modulating mitochondrial morphology[53, 54]. During the process of
412   transfer, mitochondria must be detached from the donor cell's mitochondrial network
413   and transferred to the recipient cell[6, 55]. Our findings indicate that Y-27632
414   enhances the number and length of individual mitochondria, thereby potentially
415   improving mitochondrial transport and energy production.
416   Various proteins involved in mitochondrial transport have been identified, including
417   Miro1, a GTPase located on the outer mitochondrial membrane that regulates
418   mitochondrial movement and distribution by coordinating interactions with actin and
419   microtubules[39, 45, 46]. Knockdown of Miro1 has been shown to impede
420   microtubule-dependent mitochondrial movement, underscoring its importance in this
421   process[46]. Furthermore, disruption of F-actin has been found to hinder
422   mitochondrial penetration into the cortical cytoskeleton. It is plausible that Y-27632
423   promotes mitochondrial movement and penetration by enhancing mitochondrial
424   membrane localization and stimulating microtubule polymerization. These findings
425   unveil novel mechanisms through which Y-27632 modulates intercellular
426   mitochondrial transfer and subcellular distribution.
427   Our data, along with existing research, provide support for the hypothesis that
428   Y-27632 enhances the likelihood of tunneling nanotube (TNT) formation through the
429   modulation of cytoskeletal dynamics, leading to an increase in microtubule-mediated
430   mitochondrial transport. These alterations are implicated in the facilitation of
431   TNT-mediated intercellular transfer of mitochondria. Future experiments are
432   necessary to elucidate the specific molecular mechanisms underlying the regulatory
433   effects of Y-27632 on the cytoskeleton.
434
435   **Conclusions**
436
437   In summary, our study presents novel findings indicating that Y-27632 enhances
438   the formation of tunneling nanotubes (TNTs) through its regulation of the
439   cytoskeleton. Furthermore, we observed that Y-27632 influences mitochondrial
440   distribution and transport by modulating microtubule polymerization and the
441   mitochondrial transporter protein miro1. These results offer valuable insights for the
442   advancement of TNT-mediated material exchange, particularly in the context of
443   mitochondrial transfer, as a potential therapeutic strategy. By bolstering the
444   endogenous mechanisms that facilitate TNT-mediated material transport, this
445   approach holds promise for future therapeutic interventions.
446
447   **Methods**
448
449   *Cell cultures*
450

1

451   ARPE19 cells (ATCC, #CRL-2302) were cultured in DMEM/F12 (Gibco,
452 #C11330500BT) medium supplemented with 10% fetal bovine serum (FBS)
453 (VivaCell, #C04002-500) and 1% penicillin and streptomycin (Gibco, #15140-122).
454 The cells were cultured in a humidified incubator at a temperature of 37°C with 5%
455 CO_2.

456

457 *Cell labeling*

458

459   Cells were subjected to staining using Cell Trace Violet (Invitrogen, #C34557) in
460 DPBS at a concentration of 10μM for 10 minutes at 37°C, followed by three washes
461 with fresh medium.

462

463 *Construction of ARPE19 cell line with mitochondrial fluorescent labeling*

464

465   ARPE19 cells were transduced with lentiviral vectors containing mitochondria
466 tagged with GFP (Mito-COX8-GFP, SBI, #Cyto102-PA-1) or RFP (derived from
467 Mito-COX8-GFP) to establish the ARPE19-mito-GFP and ARPE19-mito-RFP cell
468 lines, as previously described[1].

469

470 *ROCK inhibitors treatment*

471

472   ARPE19 cells were exposed to varying concentrations of Y-27632 (Selleck,
473 #S1049) including 0μM, 10μM, 20μM, 40μM, 100μM, 400μM, and 1000μM for a
474 duration of 24 hours. Y-39983 (AbMole, #M5123, 10μM) and GSK269962A
475 (Baiaolaibo, M02736, 10μM) were similarly used to treat ARPE19 cells for a duration
476 of 24 hours.

477

478 *Cell co-culture*

479

480   ARPE19-mito-GFP cells were seeded at a density of 1×10^4 cells in a single well
481 of a 24-well plate and co-cultured with either ARPE19 or ARPE19-mito-RFP cells at
482 a 1:1 ratio. The co-culture was then treated with 40μM Y27632 for a duration of 24
483 hours.

484

485 *Transwell co-culture*

486

487   ARPE19-mito-GFP cells were seeded on the upper chamber, while ARPE19 cells
488 were seeded on the lower chamber of a transwell system (Corning, #3470) with
489 0.4μm pore size inserts. Both cell types were seeded at a density of 1×10^4 cells per
490 chamber and were co-cultured for 24 hours with the treatment of 40μM Y-27632.

491

492 *Quantification of Y-NTs and mitochondrial transfer rate*

493

494   The quantification of TNTs was conducted in over 10 fields randomly selected
495 from each sample. The results are presented as the ratio of intercellular nanotubes
496 (Y-NTs) relative to the total number of cells counted in each experimental condition.
497 The presence of mitochondria from donor cells in recipient cells labeled with cell
498 trace violet was used to determine the rate of mitochondrial transfer among cells.

499

500 *Cytoskeleton staining and confocal microscopy*

501

502   Cells were cultured in a 24-well plate with coverslips for 24 hours, followed by
503 PBS washing and fixation in 4% paraformaldehyde for 30 minutes at room
504 temperature. Actin filaments (F-actin) and microtubules were stained using Phalloidin
505 (Thermo Fisher Scientific, #A22287) and anti-α-Tubulin antibody (1:500, Sigma,
506 #T9026). Samples were observed using an Olympus microscope, with STED images
507 were acquired using Abberior STEDYCON (Abberior Instruments GmbH, Göttingen,
508 Germany) fluorescence microscope built on a motorized inverted microscope IX83
509 (Olympus UPlanXAPO 100x, NA1.45, Tokyo, Japan). Cell size and nanotube length
510 were quantified using Olympus confocal software.

511

512 *Live cell imaging*

513

514   Cover-glass chambers were used for culturing ARPE19 cells.After rinsing with
515 warm PBS and changing to phenol red-free DMEM/F12 medium (Gibco, #11039021),
516 live cell imaging was conducted using an Olympus microscope equipped with a 40X
517 objective in a live cell imaging incubator set at 37°C with 5% CO_2.

518

519 *Scanning electron microscope (SEM)*

520

521   Cells (4×10^4cells/well) were cultured in a 12-well plate with a coverslip for 24
522 hours. Subsequently, the samples were fixed with 2.5% glutaraldehyde (Solarbio,
523 #P1126) for 30 minutes at room temperature and then stored at 4°C for over 8 hours.
524 Following fixation, the samples underwent a series of washes with DPBS before
525 dehydration. The dehydration protocol involved sequential immersion in 30%, 50%,
526 70%, 85%, 95%, and 100% ethanol for specific durations. Post-fixation and
527 dehydration, the coverslips were air-dried and subjected to metal coating using an
528 E-1045 ion sputtering apparatus. Imaging was performed using a HITACHI SU8010
529 microscope.

530

531 *Depolymerization of F-actin and microtubule*

532

533   To assess the impact of F-actin and microtubules on the formation of nanotubes
534 and mitochondrial transfer, cells were exposed to Cytochalasin B (MCE, #HY-16928,

535   10µM, 24 h) or Nocodazole (Sigma, #M1404, 50µM, 24h) to disturb F-actin or
536   microtubule polymerization, respectively.
537
538   *Assessment of cell apoptosis*
539
540   Apoptosis was assessed by the AnnexinV-FITC/PI apoptosis double staining kit
541   (BD, #556547). Cells were harvested, washed, and stained with 5 µl of
542   AnnexinV-FITC for 15 minutes, after which they were exposed to 5 µl of PI for 5
543   minutes. Flow cytometry was utilized for result analysis.
544
545   *Establishment of an in vitro mitochondrial injury model by light damage and*
546   *co-culture system*
547
548   ARPE19 cells were exposed to 19 klux blue light (330-340 nm) for varying
549   durations (0, 0.5, 1, 1.5, 2, and 2.5 hours) to investigate mitochondrial dysfunction. A
550   2-hour exposure to blue light was chosen to induce a model of mitochondrial injury.
551   Light-damaged and undamaged ARPE19 cells were co-cultured with healthy ARPE19
552   cells at a 1:1 ratio.
553
554   *Assessment of mitochondrial membrane potential*
555
556   Mitochondrial membrane potential assay was performed using the MitoProbe™
557   JC-1 Assay Kit (Invitrogen, #M34152). Cells were treated with JC-1 staining solution
558   for 20 minutes at 37°C, washed thrice with DPBS, and the fluorescence signal was
559   analyzed via flow cytometry.
560
561   *Oxygen consumption rate (OCR)*
562
563   The oxygen consumption rate (OCR) is a measure of the rate at which cells
564   utilize oxygen. Mitochondrial function of ARPE19 cells was assessed using a
565   seahorse XFp analyzer (Agilent Technologies). By sequentially administering drugs
566   targeting the mitochondrial electron transport chain (ETC), key parameters indicative
567   of mitochondrial function were obtained: (1) basal respiration, reflecting cellular
568   energy demand in the resting state; (2) ATP production, determined by the reduction
569   in oxygen consumption upon addition of 1.5 µM oligomycin, indicating
570   mitochondrial ATP synthesis capacity; (3) Maximum mitochondrial respiratory
571   capacity, calculated as the peak oxygen consumption following treatment with 0.5 µM
572   uncoupling agent FCCP, representing the maximal respiratory rate achievable by the
573   cells. (4) Non-mitochondrial respiration was assessed by inhibiting mitochondrial
574   respiration with a combination of 2µM rotenone and antimycin A. (5) Spare
575   respiratory capacity, defined as the difference between maximum and basal respiration,
576   signifies the cell's ability to respond to increased energy demands.

RT-qPCR

Total RNA extraction was performed using the Total RNA Extraction Kits (Fastagen, #220010). Reverse transcription was done using the HiScript III RT SuperMix for qPCR (+gDNA wiper) (Vazyme, #R323). Quantitative PCR was then performed using the AceQ qPCR SYBR Green Master Mix (Vazyme, #Q131). The primers used for miro1 as a reference gene were as follows: forward 5'-TGT TCA GCG AAA AAC CTGAA-3', reverse 5'-TTC AGC ATC ATT GAG AGTACC A-3'.

RNA-sequencing (RNA-seq)

All the RNA-seq samples were sequenced by the Illumina NovaSeq 6000 with read lengths of 150bp at opposite ends. All reads were mapped to Homo sapiens.GRCh38.94.chr with the default settings. Read counts were calculated using the FeatureCount. The cytoskeletal gene expression was calculated by the edgeR ($|\log 2\ \text{KD/NC}| > 1$, $P < 0.05$).

Western Blot

Cells were lysed in RIPA lysis buffer (Proteintech, #PR20001) supplemented with cOmplete, EDTA-free, EASY pack (Roche, 04693132001). The primary antibodies employed were anti-F-actin (1:500, Abcam, #ab205), anti-α-Tubulin (1:500, Sigma, #T9026), anti-Miro1 (1:500, Invitrogen, #PA5-42646), Goat anti-Mouse HRP (1:1000, Proteintech, #SA0001-1), and Goat anti-Rabbit HRP (1:1000, Proteintech, #SA0001-2).

Morphometric analysis of the mitochondrial network

Mitochondrial morphology analysis and quantification were conducted as previously outlined[56]. Image preprocessing was carried out to enhance contrast, clarity, and background reduction for improved binarization. The binary image was then skeletonized using the 'skeletonize' function in ImageJ. The MINA macro extracted branch lengths and numbers from the Analyze Skeleton plugin output to compute parameters characterizing mitochondrial network morphology. Mitochondrial structures were categorized as "individuals" (punctate, rod-shaped, large/circular) or "network" (≥3 branches) (Figure S5C).

Statistical analyses

Data were presented as mean±SEM or median ± interquartile rangeand analyzed with one- or two-way analysis of variance (ANOVA), Kruskal-Wallis test, Student's

619   t-test or Mann-Whitney test using SPSS 25. A P-value of < 0.05 was considered as
620   significant; ns, not significant.
621
622   **List of abbreviations**
623
624   ROCK   Rho-associated kinase
625   TNT   Tunneling nanotubes
626   RPE   Retinal pigment epithelial
627   ARPE19   Adult Retinal Pigment Epithelial cell line-19
628   MSCs   Mesenchymal stem cells
629   GFP   Green fuorescent protein
630   CM   Cytoplasmic membrane
631   RFP   Red fuorescent protein
632   Y-NTs   Y-27632-induced nanotubes
633   Cyto B   Cytochalasin B
634   Noco   Nocodazole
635   DMSO   Dimethyl sulfoxide
636

644

645   **Author contributions**
646   ZBJ and DJ were responsible for generating ideas, designing studies; ZBJ
647 supervising projects, and providing financial supports. JY was in charge of designing
648 and conducting experiments as well as analyzing and interpreting the data. FXC, ZHX,
649 and HZ performed the experiments. JY and ZBJ wrote and revised the manuscript.
650

651   **Competing interests**
652   The authors declare that they possess no competing interests.
653

654   **References**
655 1.   Jiang D, Chen FX, Zhou H, Lu YY, Tan H, Yu SJ, et al. Bioenergetic Crosstalk between
656 Mesenchymal Stem Cells and various Ocular Cells through the intercellular trafficking of Mitochondria.
657 Theranostics. 2020; 10: 7260-72.
658 2.   Yin P, Li Y, Lv H, Deng Y, Meng Y, Zhang L, et al. Exchange of genetic material: a new paradigm
659 in bone cell communications. Cell Mol Life Sci. 2018; 75: 1989-98.

660   3.   Li Q, Wang M, Liu L. The role of exosomes in the stemness maintenance and progression of acute
661   myeloid leukemia. Biochem Pharmacol. 2023; 212: 115539.

662   4.   Mittelbrunn M, Sánchez-Madrid F. Intercellular communication: diverse structures for exchange
663   of genetic information. Nat Rev Mol Cell Biol. 2012; 13: 328-35.

664   5.   Shanmughapriya S, Langford D, Natarajaseenivasan K. Inter and Intracellular mitochondrial
665   trafficking in health and disease. Ageing Res Rev. 2020; 62: 101128.

666   6.   Liu Y, Fu T, Li G, Li B, Luo G, Li N, et al. Mitochondrial transfer between cell crosstalk - An
667   emerging role in mitochondrial quality control. Ageing Res Rev. 2023; 91: 102038.

668   7.   Qin Y, Jiang X, Yang Q, Zhao J, Zhou Q, Zhou Y. The Functions, Methods, and Mobility of
669   Mitochondrial Transfer Between Cells. Front Oncol. 2021; 11: 672781.

670   8.   Al Amir Dache Z, Thierry AR. Mitochondria-derived cell-to-cell communication. Cell Rep. 2023;
671   42: 112728.

672   9.   Annesley SJ, Fisher PR. Mitochondria in Health and Disease. Cells. 2019; 8.

673   10.   Nunnari J, Suomalainen A. Mitochondria: in sickness and in health. Cell. 2012; 148: 1145-59.

674   11.   Geng Z, Guan S, Wang S, Yu Z, Liu T, Du S, et al. Intercellular mitochondrial transfer in the brain,
675   a new perspective for targeted treatment of central nervous system diseases. CNS Neurosci Ther. 2023;
676   29: 3121-35.

677   12.   Fairley LH, Grimm A, Eckert A. Mitochondria Transfer in Brain Injury and Disease. Cells. 2022;
678   11.

679   13.   Wei B, Ji M, Lin Y, Wang S, Liu Y, Geng R, et al. Mitochondrial transfer from bone mesenchymal
680   stem cells protects against tendinopathy both in vitro and in vivo. Stem Cell Res Ther. 2023; 14: 104.

681   14.   Hu X, Duan T, Wu Z, Xiong Y, Cao Z. Intercellular mitochondria transfer: a new perspective for
682   the treatment of metabolic diseases. Acta Biochim Biophys Sin (Shanghai). 2021; 53: 958-60.

683   15.   Liu D, Gao Y, Liu J, Huang Y, Yin J, Feng Y, et al. Intercellular mitochondrial transfer as a means
684   of tissue revitalization. Signal Transduct Target Ther. 2021; 6: 65.

685   16.   Borcherding N, Brestoff JR. The power and potential of mitochondria transfer. Nature. 2023; 623:
686   283-91.

687   17.   Paliwal S, Chaudhuri R, Agrawal A, Mohanty S. Regenerative abilities of mesenchymal stem cells
688   through mitochondrial transfer. J Biomed Sci. 2018; 25: 31.

689   18.   Rustom A, Saffrich R, Markovic I, Walther P, Gerdes HH. Nanotubular highways for intercellular
690   organelle transport. Science. 2004; 303: 1007-10.

691   19.   Spees JL, Olson SD, Whitney MJ, Prockop DJ. Mitochondrial transfer between cells can rescue
692   aerobic respiration. Proc Natl Acad Sci U S A. 2006; 103: 1283-8.

693   20.   Drab M, Stopar D, Kralj-Iglič V, Iglič A. Inception Mechanisms of Tunneling Nanotubes. Cells.
694   2019; 8.

695   21.   Zhang J, Zhang Y. Membrane nanotubes: novel communication between distant cells. Sci China
696   Life Sci. 2013; 56: 994-9.

697   22.   Cordero Cervantes D, Zurzolo C. Peering into tunneling nanotubes-The path forward. Embo j.
698   2021; 40: e105789.

699   23.   Dagar S, Pathak D, Oza HV, Mylavarapu SVS. Tunneling nanotubes and related structures:
700   molecular mechanisms of formation and function. Biochem J. 2021; 478: 3977-98.

701 24.   Driscoll J, Gondaliya P, Patel T. Tunneling Nanotube-Mediated Communication: A Mechanism of
702 Intercellular Nucleic Acid Transfer. Int J Mol Sci. 2022; 23.

703 25.   Abounit S, Zurzolo C. Wiring through tunneling nanotubes--from electrical signals to organelle
704 transfer. J Cell Sci. 2012; 125: 1089-98.

705 26.   Ariazi J, Benowitz A, De Biasi V, Den Boer ML, Cherqui S, Cui H, et al. Tunneling Nanotubes
706 and Gap Junctions-Their Role in Long-Range Intercellular Communication during Development,
707 Health, and Disease Conditions. Front Mol Neurosci. 2017; 10: 333.

708 27.   Li CJ, Chen PK, Sun LY, Pang CY. Enhancement of Mitochondrial Transfer by Antioxidants in
709 Human Mesenchymal Stem Cells. Oxid Med Cell Longev. 2017; 2017: 8510805.

710 28.   Cheng XY, Biswas S, Li J, Mao CJ, Chechneva O, Chen J, et al. Human iPSCs derived astrocytes
711 rescue rotenone-induced mitochondrial dysfunction and dopaminergic neurodegeneration in vitro by
712 donating functional mitochondria. Transl Neurodegener. 2020; 9: 13.

713 29.   Nasoni MG, Carloni S, Canonico B, Burattini S, Cesarini E, Papa S, et al. Melatonin reshapes the
714 mitochondrial network and promotes intercellular mitochondrial transfer via tunneling nanotubes after
715 ischemic-like injury in hippocampal HT22 cells. J Pineal Res. 2021; 71: e12747.

716 30.   Lin TK, Chen SD, Chuang YC, Lan MY, Chuang JH, Wang PW, et al. Mitochondrial Transfer of
717 Wharton's Jelly Mesenchymal Stem Cells Eliminates Mutation Burden and Rescues Mitochondrial
718 Bioenergetics in Rotenone-Stressed MELAS Fibroblasts. Oxid Med Cell Longev. 2019; 2019:
719 9537504.

720 31.   Ahmad T, Mukherjee S, Pattnaik B, Kumar M, Singh S, Kumar M, et al. Miro1 regulates
721 intercellular mitochondrial transport & enhances mesenchymal stem cell rescue efficacy. Embo j. 2014;
722 33: 994-1010.

723 32.   Ljubojevic N, Henderson JM, Zurzolo C. The Ways of Actin: Why Tunneling Nanotubes Are
724 Unique Cell Protrusions. Trends Cell Biol. 2021; 31: 130-42.

725 33.   Yuan XB, Jin M, Xu X, Song YQ, Wu CP, Poo MM, et al. Signalling and crosstalk of Rho
726 GTPases in mediating axon guidance. Nat Cell Biol. 2003; 5: 38-45.

727 34.   Kalargyrou AA, Basche M, Hare A, West EL, Smith AJ, Ali RR, et al. Nanotube-like processes
728 facilitate material transfer between photoreceptors. EMBO Rep. 2021; 22: e53732.

729 35.   Hanna SJ, McCoy-Simandle K, Miskolci V, Guo P, Cammer M, Hodgson L, et al. The Role of
730 Rho-GTPases and actin polymerization during Macrophage Tunneling Nanotube Biogenesis. Sci Rep.
731 2017; 7: 8547.

732 36.   Delage E, Cervantes DC, Pénard E, Schmitt C, Syan S, Disanza A, et al. Differential identity of
733 Filopodia and Tunneling Nanotubes revealed by the opposite functions of actin regulatory complexes.
734 Sci Rep. 2016; 6: 39632.

735 37.   Scaife RM, Job D, Langdon WY. Rapid microtubule-dependent induction of neurite-like
736 extensions in NIH 3T3 fibroblasts by inhibition of ROCK and Cbl. Mol Biol Cell. 2003; 14: 4605-17.

737 38.   Wittig D, Wang X, Walter C, Gerdes HH, Funk RH, Roehlecke C. Multi-level communication of
738 human retinal pigment epithelial cells via tunneling nanotubes. PLoS One. 2012; 7: e33195.

739 39.   Boldogh IR, Pon LA. Mitochondria on the move. Trends Cell Biol. 2007; 17: 502-10.

740 40.   MacAskill AF, Kittler JT. Control of mitochondrial transport and localization in neurons. Trends
741 Cell Biol. 2010; 20: 102-12.

742 41. Xu ZH, Zhang H, Zhang CJ, Yu SJ, Yuan J, Jin K, et al. REG1A protects retinal photoreceptors

743 from blue light damage. Ann N Y Acad Sci. 2023; 1527: 60-74.

744 42. Keller KE, Bradley JM, Sun YY, Yang YF, Acott TS. Tunneling Nanotubes are Novel Cellular

745 Structures That Communicate Signals Between Trabecular Meshwork Cells. Invest Ophthalmol Vis Sci.

746 2017; 58: 5298-307.

747 43. Caino MC, Ghosh JC, Chae YC, Vaira V, Rivadeneira DB, Faversani A, et al. PI3K therapy

748 reprograms mitochondrial trafficking to fuel tumor cell invasion. Proc Natl Acad Sci U S A. 2015; 112:

749 8638-43.

750 44. Castro IG, Schrader M. Miro1 - the missing link to peroxisome motility. Commun Integr Biol.

751 2018; 11: e1526573.

752 45. López-Doménech G, Howden JH, Covill-Cooke C, Morfill C, Patel JV, Bürli R, et al. Loss of

753 neuronal Miro1 disrupts mitophagy and induces hyperactivation of the integrated stress response.

754 Embo j. 2021; 40: e100715.

755 46. López-Doménech G, Covill-Cooke C, Ivankovic D, Halff EF, Sheehan DF, Norkett R, et al. Miro

756 proteins coordinate microtubule- and actin-dependent mitochondrial transport and distribution. Embo j.

757 2018; 37: 321-36.

758 47. Mittal R, Karhu E, Wang JS, Delgado S, Zukerman R, Mittal J, et al. Cell communication by

759 tunneling nanotubes: Implications in disease and therapeutic applications. J Cell Physiol. 2019; 234:

760 1130-46.

761 48. Scheiblich H, Dansokho C, Mercan D, Schmidt SV, Bousset L, Wischhof L, et al. Microglia

762 jointly degrade fibrillar alpha-synuclein cargo by distribution through tunneling nanotubes. Cell. 2021;

763 184: 5089-106.e21.

764 49. Jiang D, Xu W, Peng F, Sun Y, Pan C, Yu J, et al. Tunneling nanotubes-based intercellular

765 mitochondrial trafficking as a novel therapeutic target in dry eye. Exp Eye Res. 2023; 232: 109497.

766 50. Wang X, Gerdes HH. Transfer of mitochondria via tunneling nanotubes rescues apoptotic PC12

767 cells. Cell Death Differ. 2015; 22: 1181-91.

768 51. O'Leary F, Campbell M. The blood-retina barrier in health and disease. Febs j. 2023; 290: 878-91.

769 52. Cunniff B, McKenzie AJ, Heintz NH, Howe AK. AMPK activity regulates trafficking of

770 mitochondria to the leading edge during cell migration and matrix invasion. Mol Biol Cell. 2016; 27:

771 2662-74.

772 53. Whitley BN, Engelhart EA, Hoppins S. Mitochondrial dynamics and their potential as a

773 therapeutic target. Mitochondrion. 2019; 49: 269-83.

774 54. Adebayo M, Singh S, Singh AP, Dasgupta S. Mitochondrial fusion and fission: The fine-tune

775 balance for cellular homeostasis. Faseb j. 2021; 35: e21620.

776 55. Chan DC. Mitochondrial Dynamics and Its Involvement in Disease. Annu Rev Pathol. 2020; 15:

777 235-59.

778 56. Valente AJ, Maddalena LA, Robb EL, Moradi F, Stuart JA. A simple ImageJ macro tool for

779 analyzing mitochondrial network morphology in mammalian cell culture. Acta Histochem. 2017; 119:

780 315-26.

781

Figures

783
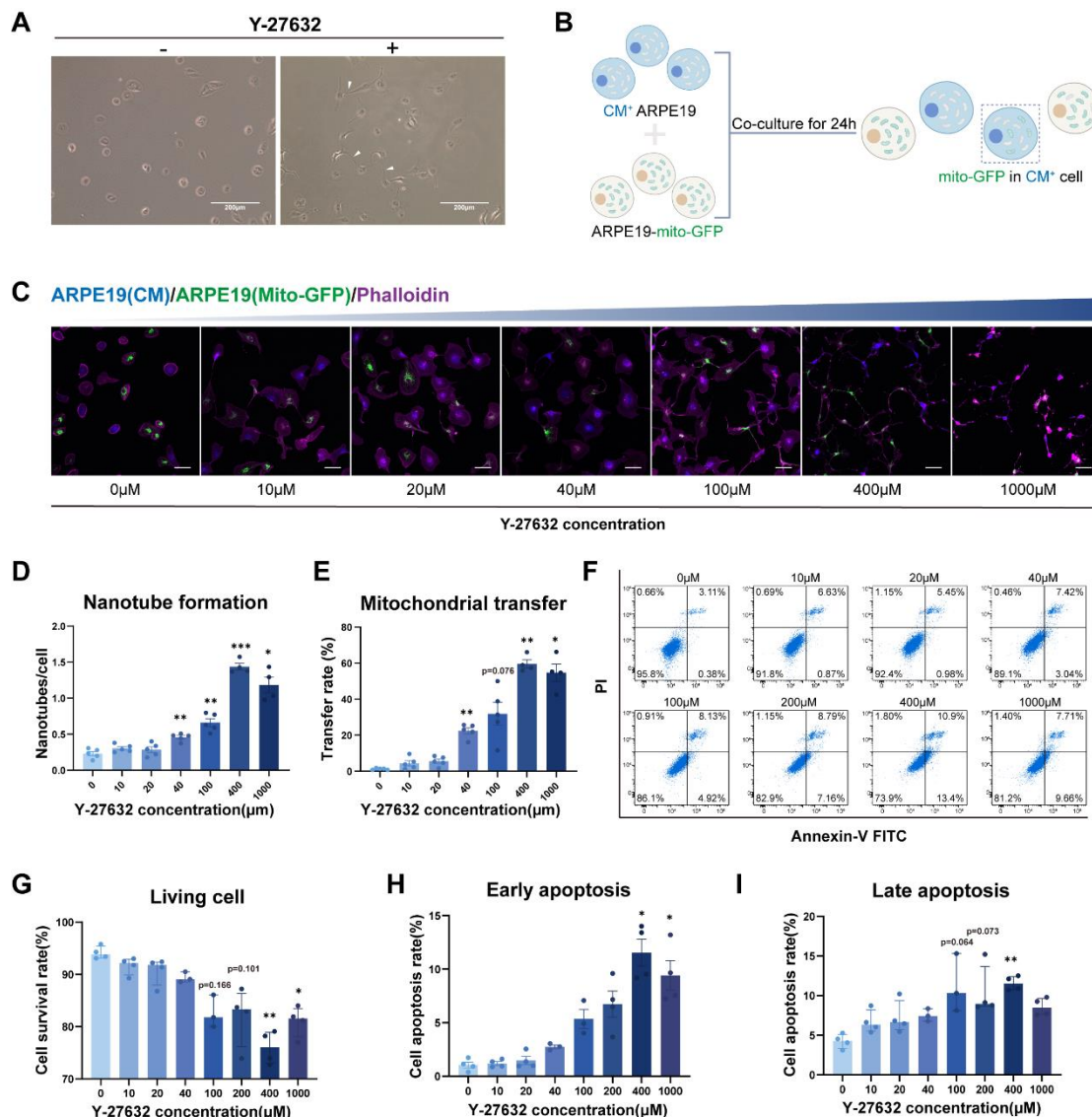
Figure 1. Y-27632-induced intercellular nanotube formation and mitochondrial transfer are dose-dependent

(A) Images captured under bright-field microscopy of nanotubes in ARPE19 cells treated with the ROCK inhibitor Y-27632 (10µM) for 24 hours are shown, with nanotubes indicated by white triangles. Scale bar: 200µm.

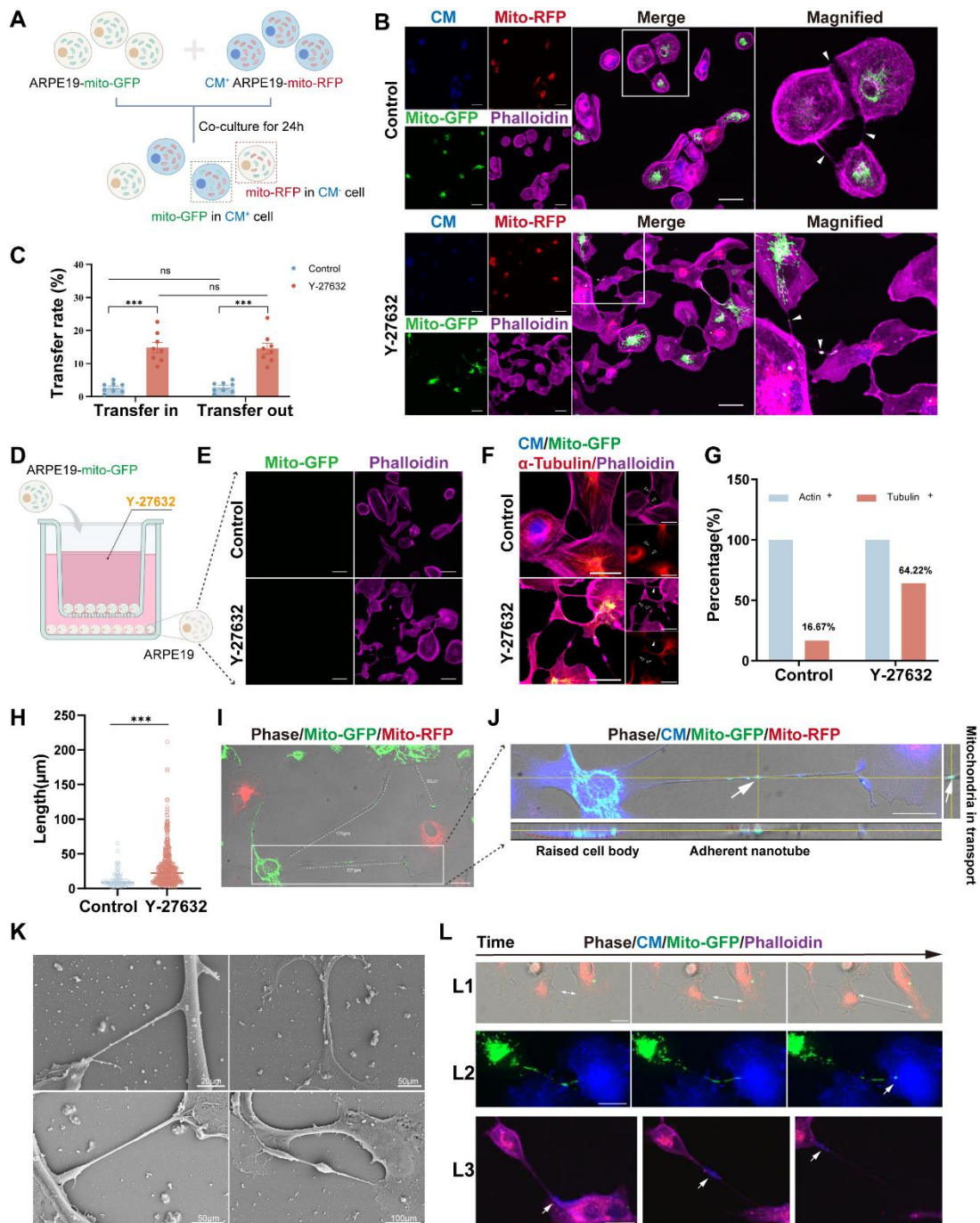(B) A diagram illustrating the co-culture program. ARPE19 cells expressing mito-GFP (green) were co-cultured as donor cells in direct contact with ARPE19 cells stained with cytoplasmic membrane (CM, blue) as recipient cells at a ratio of 1:1 for 24 hours. Mito-GFP in CM^{+} cells marked mitochondrial transfer.

(C) ARPE19-mito-GFP (green) and ARPE19 cells (CM, blue) were co-cultured and treated with varying concentrations of Y-27632 for 24 hours to induce nanotube formation. Nanotube formation and mitochondrial transfer were imaged by confocal microscopy. Scale bar: 50µm.

(D, E) The number of nanotubes each cell formed and mitochondrial transfer rate

2

were quantified. n=5, one-way ANOVA with Dunnett's T3 multiple comparisons post
800 hoc tests, mean±SEM; $*p < 0.05, **p < 0.01, ***p < 0.001$.
801 (F-I) Representative flow cytometry images of Annexin V-FITC/PI analysis for
802 ARPE19 cells with treatment of varying concentrations of Y-27632 for 24 hours (F).
803 The percentage of living cells (Annexin V-FITC$^-$/PI$^-$) (G), early apoptotic cells
804 (Annexin V-FITC$^+$/PI$^-$) (H) and late apoptotic cells (Annexin V-FITC$^+$/PI$^+$) (I) were
805 quantified. n=4, Kruskal-Wallis test,, median ± interquartile range; $*p < 0.05, **p <$
806 0.01.

807
808 **Figure 2. Characterization of Y-27632-induced nanotubes**
809 (A) A diagram illustrating the co-culture experiments. ARPE19-mito-GFP cells (green)

2

810 and ARPE19-mito-RFP cells (red, CM, blue) co-culture at 1:1 ratio for 24 hours.
811 Mito-GFP in CM$^+$ cells marked mitochondrial transfer from ARPE19-mito-GFP cells
812 to ARPE19-mito-RFP cells while mito-RFP in CM$^-$ cells marked mitochondrial
813 transfer from ARPE19-mito-RFP cells to ARPE19-mito-GFP cells.
814 (B) ARPE19-mito-RFP cells (blue) were co-cultured with ARPE19-mito-GFP cells
815 (green) for 24 hours. All cells were stained with phalloidin (magenta) followed by
816 fluorescent confocal microscopy. White triangles indicate nanotubes with or without
817 mitochondria. Scale bar: 50µm.
818 (C) Mitochondrial transfer rate including transfer in and transfer out of ARPE19 cells
819 were quantified in control and Y-27632 groups. n=8, two-way ANOVA test,
820 mean±SEM; ns, not significant,***p < 0.001.
821 (D) A diagram showing that ARPE19-mito-GFP cells (green) were co-cultured as
822 donor cells with ARPE19 as recipient cells at 1:1 ratio, with the two types of cells
823 separated by filters in transwell.
824 (E) Representative images of ARPE19 cells (phalloidin, magenta) in the bottom of a
825 transwell plate. Scale bar:50 µm.
826 (F) F-actin (phalloidin, magenta) and microtubules (α-tubulin, red) of nanotubes were
827 detected in ARPE19 cells in control and Y-27632 groups. White solid triangles
828 indicate nanotubes containing both F-actin and microtubules, while hollow triangles
829 indicate nanotubes containing F-actin, lacking microtubules. Scale bar: 50 µm.
830 (G) The percentage of nanotubes containing F-actin (actin+) and microtubules
831 (tubulin+) were quantified.n (control)=42, n (Y-27632)=218.
832 (H) Quantification of the length of intercellular nanotubes in control and Y-27632
833 groups. n (control)=91, n (Y-27632)=453. Mann-Whitney test, median ± interquartile
834 range; ***p < 0.001.
835 (I) Intercellular nanotubes of different lengths are formed between ARPE19-mito-GFP
836 and ARPE19-mito-RFP cells following treatment with Y-27632. The white dotted line
837 marks the nanotube with their length measured. Scale bar: 25 µm.
838 (J) Nanotubes shown by CM staining (blue) were adherent to the substrate (X-Z axes).
839 Scale bar: 25 µm.
840 (K) Representative images of scanning electron microscope (SEM) show different
841 kinds of Y-27632-induced intercellular nanotubes.
842 (L) Time-lapse microscopic images taken from Movie 1, 2 and 3 showing that
843 intercellular nanotube formation between ARPE19-mito-GFP (green) and
844 ARPE19-mito-RFP cells (red) (white arrows indicate the direction of cell movement)
845 (L1), mitochondrial transfer from ARPE19-mito-GFP cells (green) to ARPE19 cells
846 (blue) (L2), and some other cargoes (blue) are transported between ARPE19 cells
847 (magenta) (L3). Scale bar: 25 µm.

A

Y-27632

ARPE19(CM)/ARPE19-mito-GFP/α-Tubulin/Phalloidin

B

C
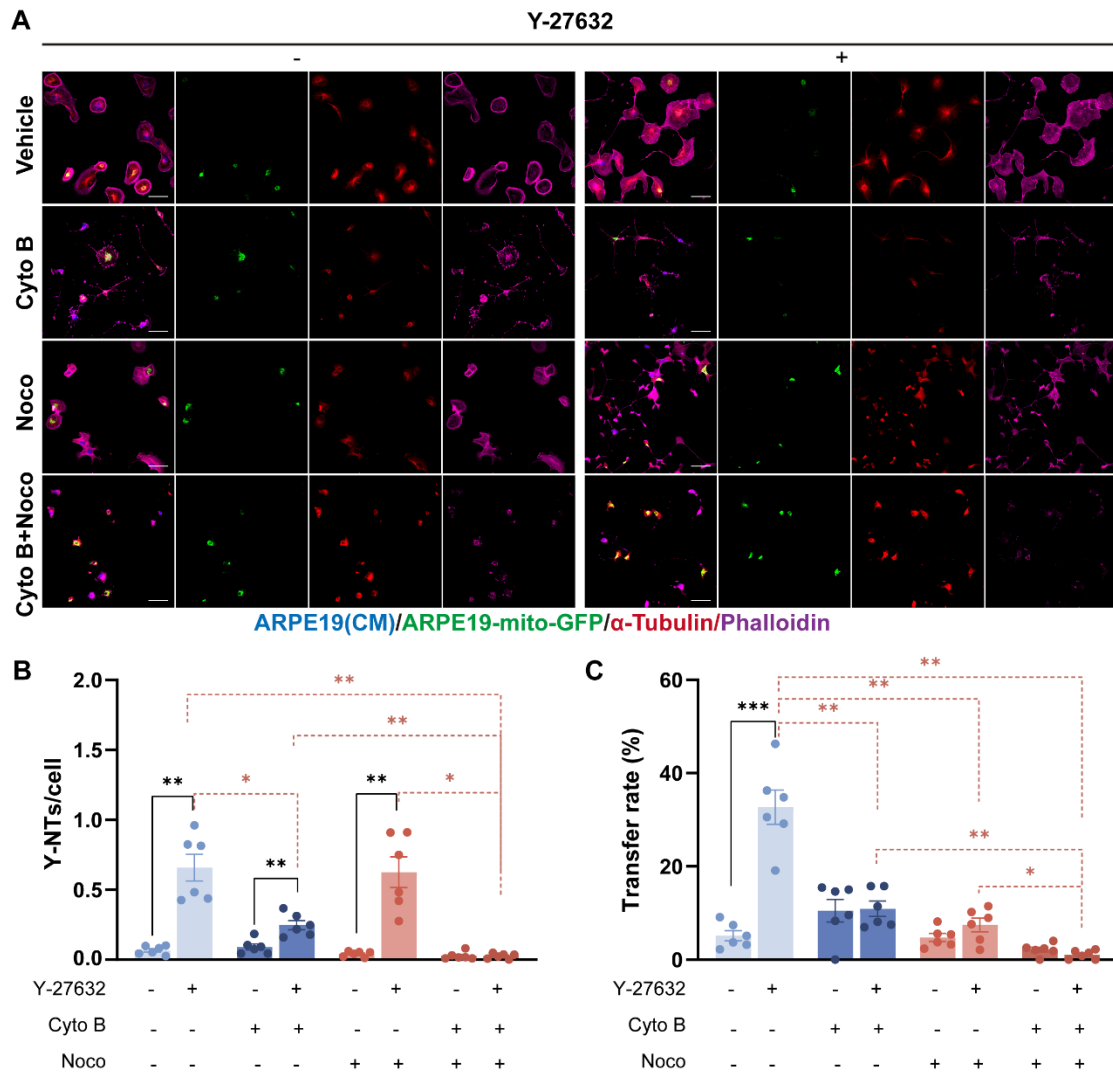
848

849 **Figure 3. Cytoskeletal inhibition eliminates Y-NTs mediated mitochondrial**
850 **transfer**

851 (A) ARPE19-mito-GFP cells (green) co-cultured with ARPE19 cells (blue) in control
852 and Y-27632 groups were treated with Cytochalasin B (CytoB) (10µM, 24h),
853 Nocodazole (Noco) (50µM, 24h) and stained with phalloidin (magenta) and
854 anti-α-tubulin antibody (red). Scale bar: 50µm.

855 (B, C) Intercellular nanotube formation and mitochondrial transfer rate were
856 quantified in each group. n=6, Comparison of the effects of different inhibitor
857 treatments on the control and Y-27632 groups was performed using t-tests, and
858 comparison of the effects of different inhibitor treatments within the control or
859 Y-27632 groups was performed using one-way ANOVA. mean±SEM; *$p < 0.05$, **p
860 < 0.01, ***$p < 0.001$. Here, we have unified the results into a single graph for ease of
861 presentation.
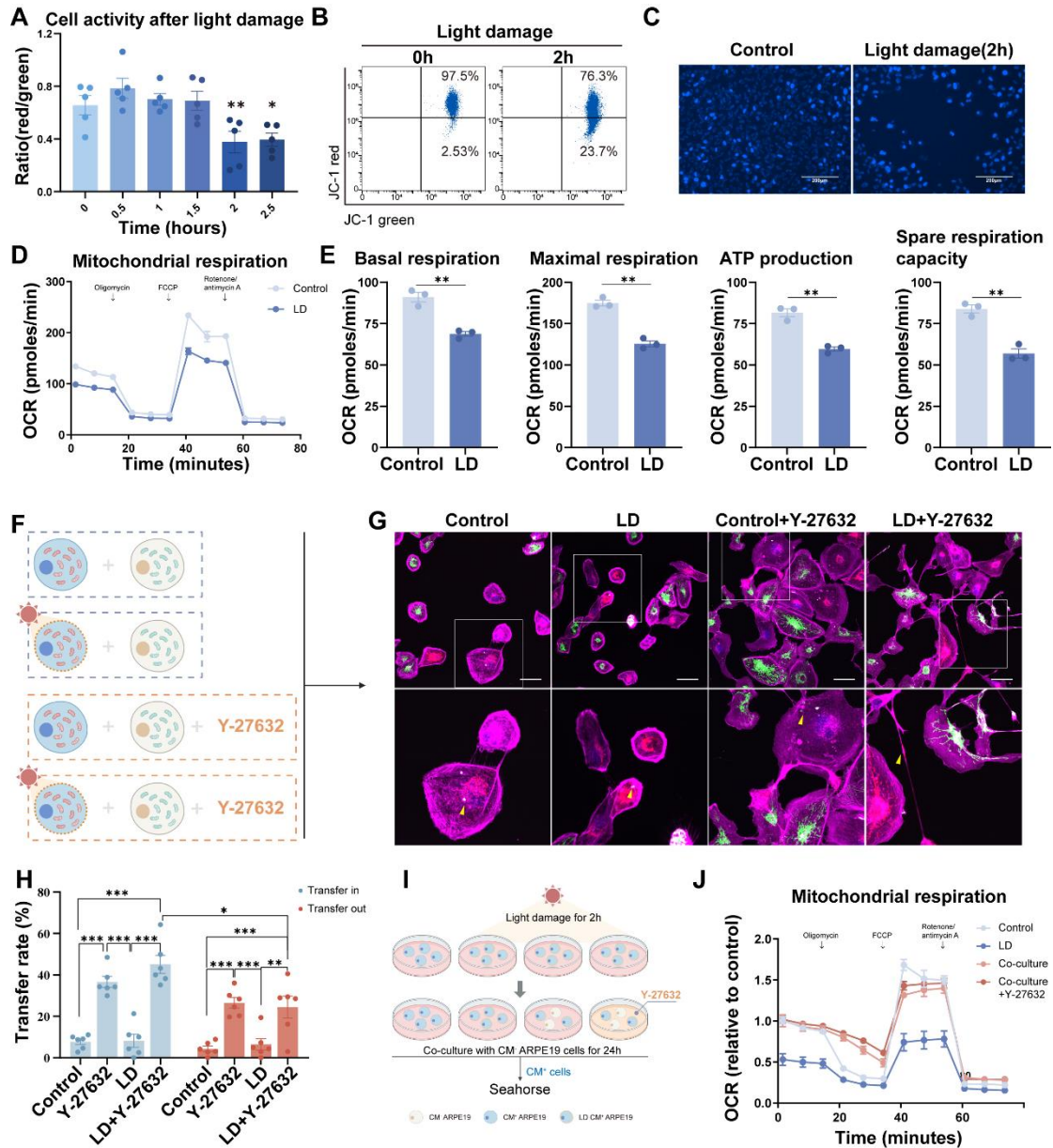
Figure 4. Y-NTs mediated mitochondrial transfer rescues light-damaged ARPE19 cells

(A) Cell activity shown as the ratio of red/green by JC-1 test with light exposure of different durations. n=5, one-way ANOVA test, mean±SEM; *p < 0.05.

(B) Representative flow cytometry plot of the result of the JC-1 test for ARPE19 cells after light damage for 0 hours and 2 hours.

(C) Representative images of Hoechst 33342 staining (blue) of ARPE19 cells after light damage for 0 hours and 2 hours. Scale bar: 200μm.

(D) Extracellular oxygen consumption rate (OCR) analysis of ARPE19 cells after 2 hours of light damage by Seahorse.

(E) Quantification of oxygen consumption rate (OCR) in mitochondrial basal respiration, maximal respiration, ATP production, and spare respiratory capacity. n=3, t-test, mean±SEM; ns, not significant,**p < 0.01.

2

876 (F) A diagram showing that CM^+ ARPE19-mito-RFP cells with or without light
877 damage were co-cultured with healthy ARPE19-mito GFP cells at a 1:1 ratio in the
878 absence or presence of Y-27632.
879 (G) Representative images of co-cultured light-damaged ARPE19-mito-RFP cells
880 (blue) with healthy ARPE19-mito GFP cells (green), all cells were stained with
881 phalloidin (magenta). Enlarged box area displaying the donor-derived mitochondria
882 (green) in recipient CM^+ cells (blue). Yellow triangles indicate mitochondrial transfer.
883 Scale bar: 50µm.
884 (H) Mitochondrial transfer rates including transfer in and transfer out of
885 light-damaged ARPE19 cells were quantified in different groups. Scale bar: 50µm.
886 n=6, Comparison of the effects of different treatments on the mitochondrial transfer
887 rate between ARPE19 cells was performed by one-way ANOVA, and t-test was used
888 to compare the mitochondrial transfer rate into and out of ARPE19 cells under the
889 same treatment., mean±SEM; ns,not significant,$*p < 0.05$,$**p < 0.01$, $***p < 0.001$.
890 Here, we have unified the results into a single graph for ease of presentation.
891 (I) A diagram showing that CM^+ ARPE19 cells with or without light damage were
892 further cultured or co-cultured with healthy ARPE19 cells at a 1:1 ratio in the absence
893 or presence of Y-27632 and analyzed by seahorse.
894 (J) Extracellular oxygen consumption rate (OCR) analysis of ARPE19 cells in
895 different groups normalized to control.
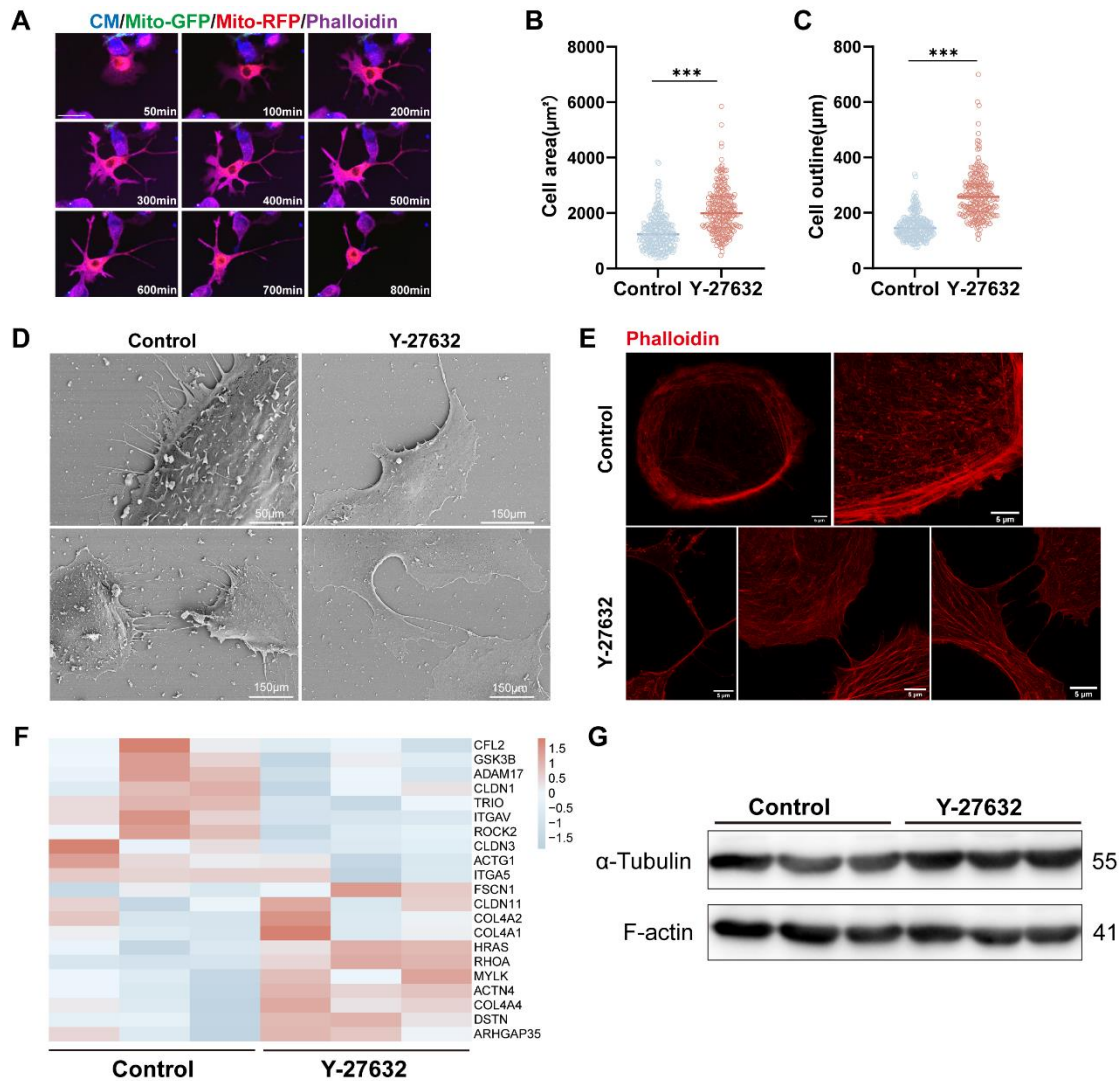
Figure 5. Y-27632 regulates cytoskeleton remodeling

(A) Time-lapse microscopic images taken from Movie 2 showing the morphological change in an ARPE19 cell (phalloidin, magenta) treated with 40µM Y-27632. Scale bar: 50µm.

(B-C) Quantitative statistics of cell area (B) and outline length (C) of ARPE19 cells in control and Y-27632 groups. n (control)=256, n (Y-27632)=228.Mann-Whitney test, median ± interquartile range; ***p < 0.001.

(D) Representative images of scanning electron microscope (SEM) show morphological differences between ARPE19 cells in control and Y-27632 groups.

(E) Super-resolution confocal imaging reveals changes in the alignment of microfilaments at the edge of the contour of Y-27632-treated ARPE19 cells. Scale bar: 5µm.

(F) Heatmap showing differences in the expression of some cytoskeletal molecules in ARPE19 cells after Y-27632 treatment, but not statistically significant.

(G) Microfilament (F-actin) and microtubule (α-tubulin) protein levels were detected in control and Y-27632 groups by Western blotting.
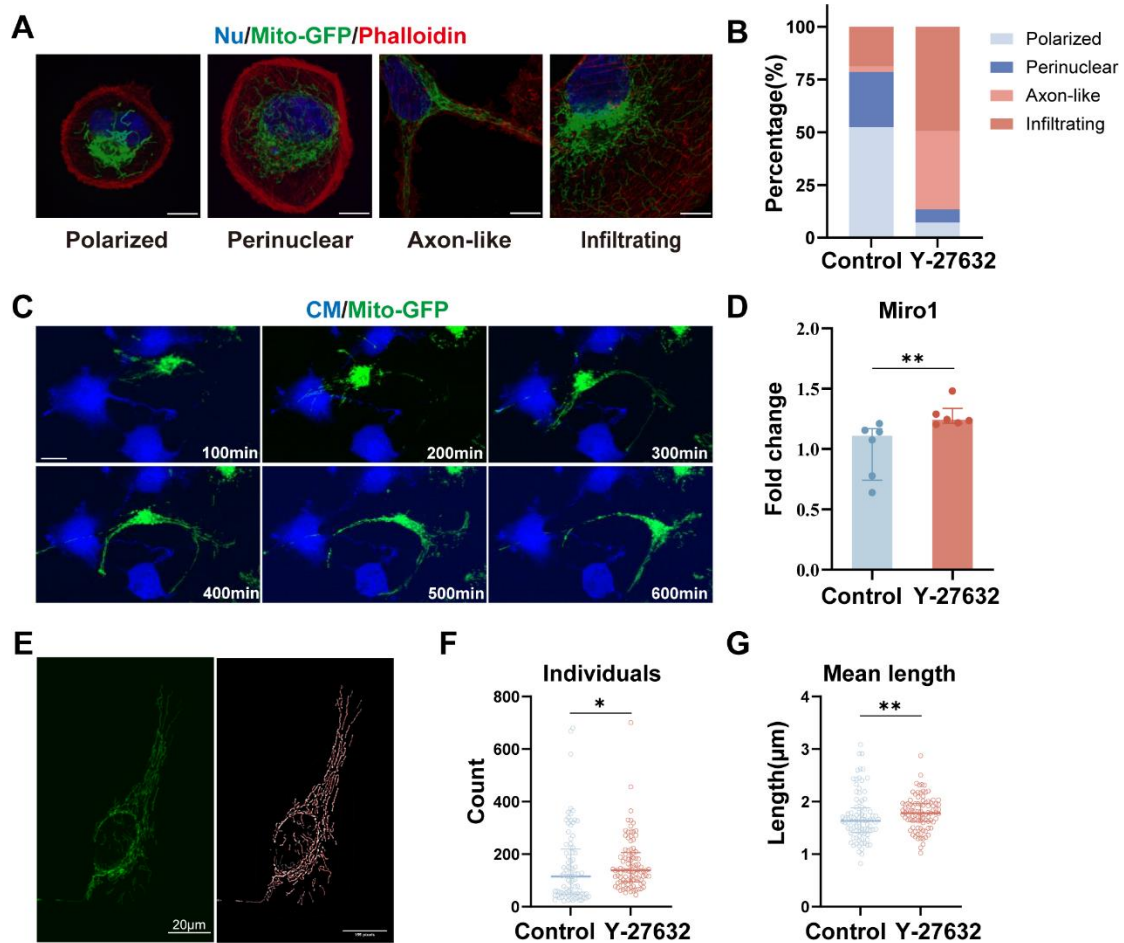
Figure 6. Y-27632 promotes mitochondrial movement in response to cytoskeletal changes

(A) Four mitochondrial distribution patterns identified by confocal microscopy. ARPE19-mito-GFP cells (green) were stained with phalloidin (red) and DAPI (blue). Images displaying different distribution patterns of mitochondrial (polarized, perinuclear, axon-like, and infiltrating). Scale bar: 25 μm.

(B) Quantifying the proportion of cells exhibiting various patterns of mitochondrial distribution (polarized, perinuclear, axon-like, and infiltrating). n (control)=107, n (Y-27632) =97.

(C) Time-lapse microscopic images taken from Movie 3 showing the movement of mitochondria (green) in an ARPE19 cell treated with 40μM Y-27632. Scale bar: 25 μm.
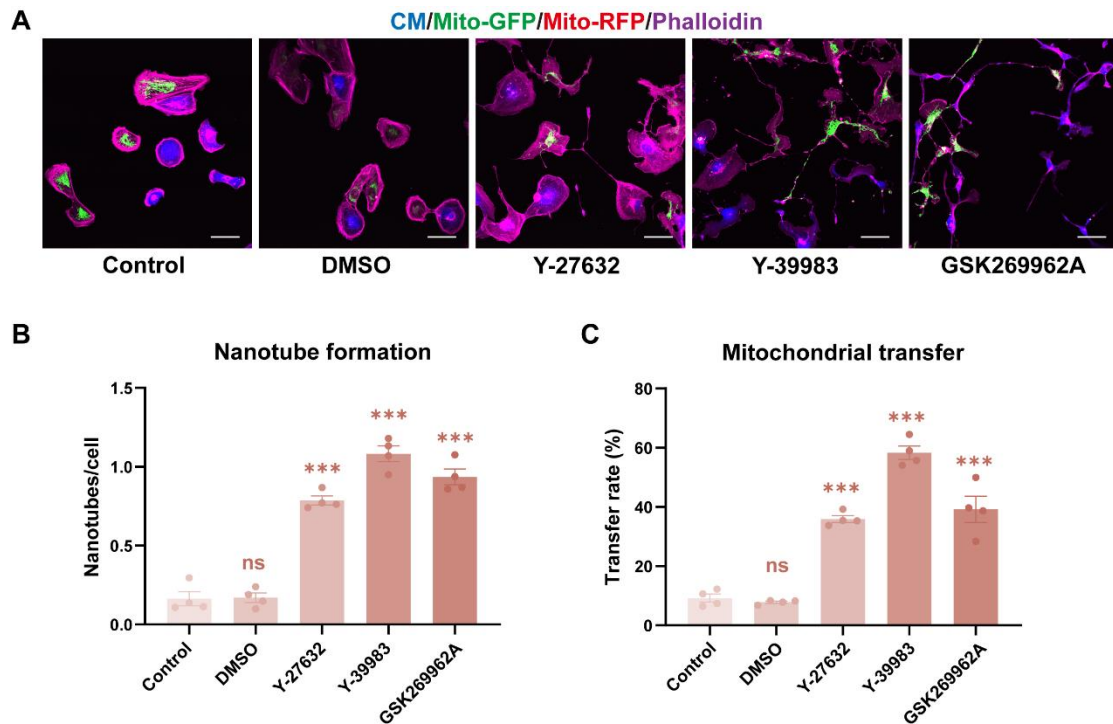
(D) Quantitative RT-PCR was performed to detect miro1 mRNA levels. n=6, Mann-Whitney test, median ± interquartile range; **$p < 0.01$.

(E) Intact mitochondria of an ARPE19-mito-GFP cell (green, left) and its mitochondrial network skeleton extracted by image J software (right). Scale bar: 20μm.

(F-G) The number and average length of individual mitochondria in control and Y-27632 groups were quantified. n (control)=88, n (Y-27632)=95. Mann-Whitney test, median ± interquartile range; *$p < 0.05$,**$p < 0.01$.

Supplemental Figures

936

A

CM/Mito-GFP/Mito-RFP/Phalloidin

Control   DMSO   Y-27632   Y-39983   GSK269962A

**B** Nanotube formation

C Mitochondrial transfer

937

Supplemental Figure 1. ROCK inhibitors-induced intercellular nanotube formation and mitochondrial transfer.

(A) Representative images of ARPE19-mito-GFP (green) and ARPE19-mito-RFP cells (CM, blue; red) co-cultured and treated with different ROCK inhibitors for 24 hours.

(B, C) The number of nanotubes each cell formed and mitochondrial transfer rate were quantified in control, DMSO, Y-27632 (40µM), Y-39983 (10µM) and GSK269962A (10µM) groups. n=8, one-way ANOVA test, mean±SEM; ns, not significant,***p < 0.001.

947

A ARPE19-mito-GFP   **B** ARPE19-mito-RFP
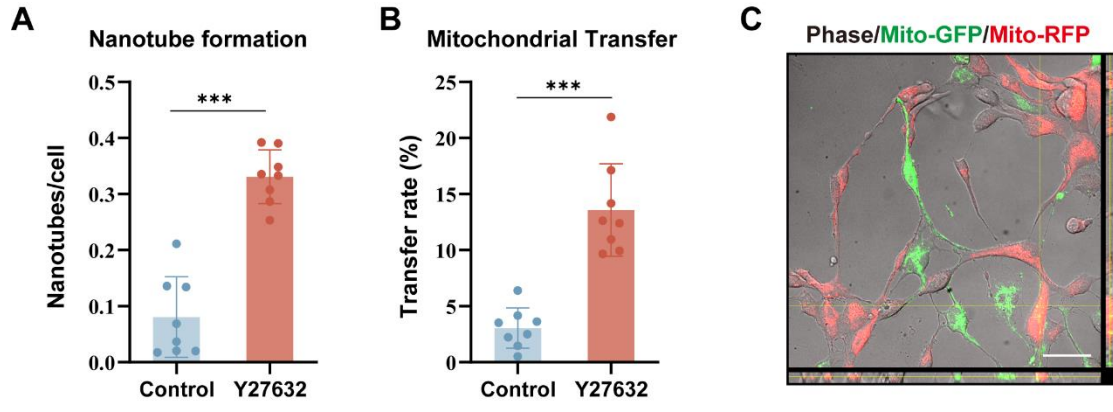
948
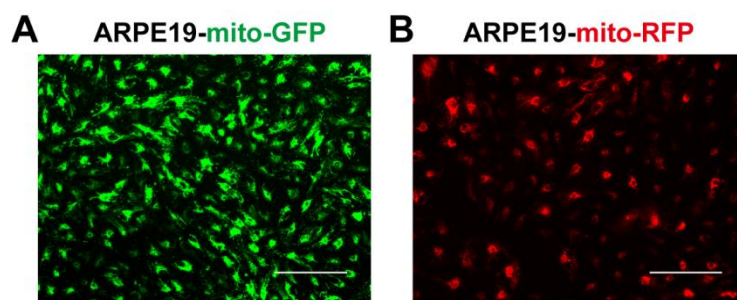
Supplemental Figure 2. Construction of mitochondrial fluorescently labeled ARPE19 cell lines

(A, B) ARPE19 cells were infected with lentivirus-containing mitochondria with GFP (mito-GFP) and RFP (mito-RFP).

953

954

Supplemental Figure 3. Characterization of Y-27632-induced nanotubes

(A, B) The number of nanotubes each cell formed and mitochondrial transfer rate were quantified in control and Y-27632 (40μM for 24 h) groups. n=8, t test, mean±SEM; ***p < 0.001.

(C)Intercellular nanotubes curved with branching are formed between ARPE19-mito-GFP and ARPE19-mito-RFP cells following treatment with Y-27632. Scale bar: 50 µm.
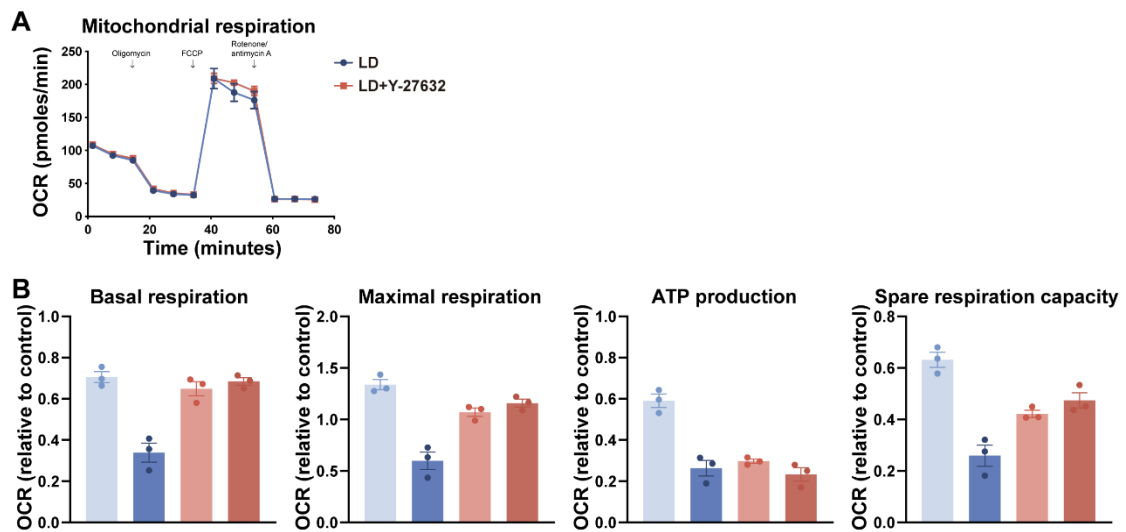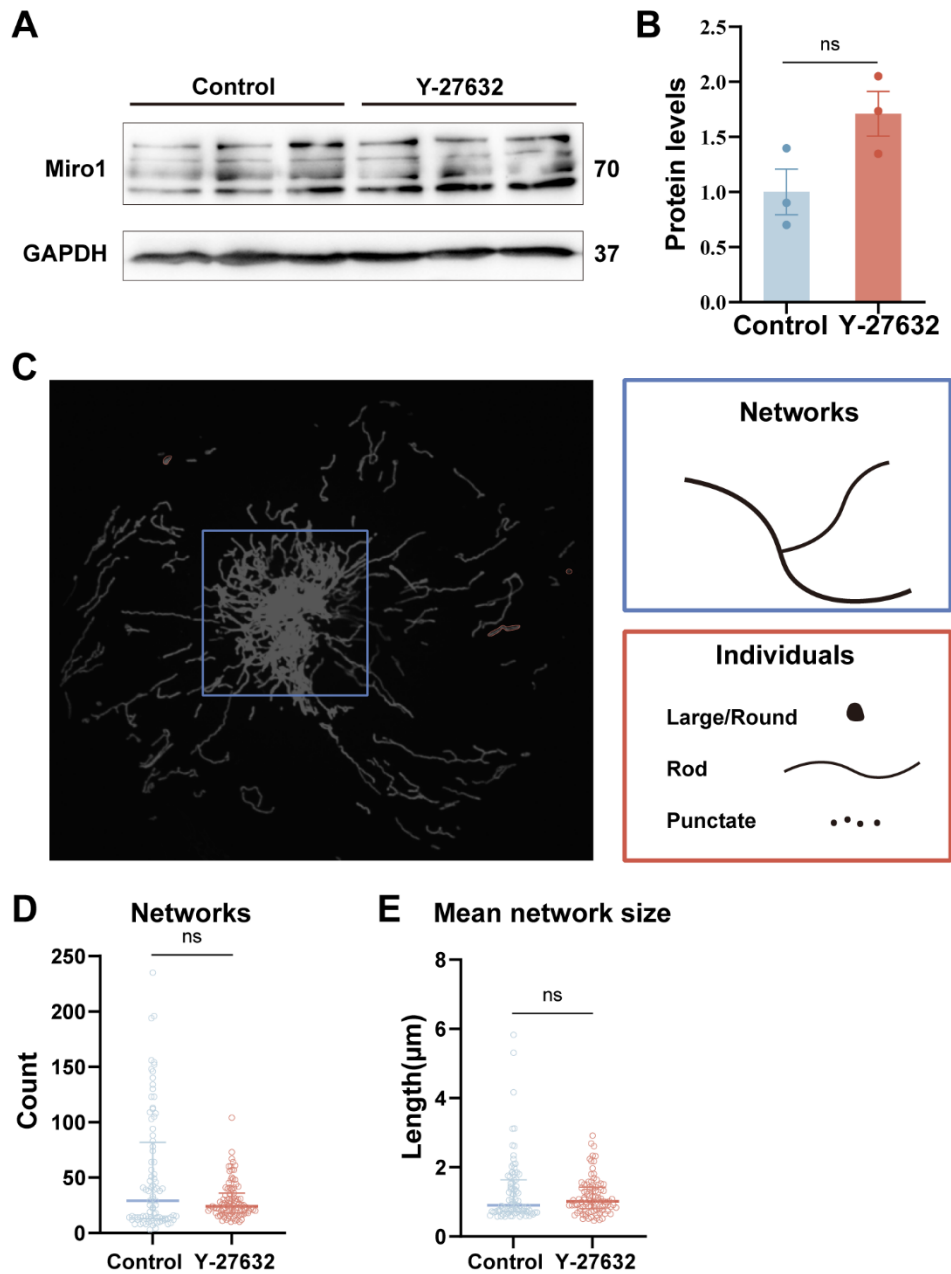

Supplemental Figure 4. Effect of Y-27632 on light-damaged ARPE19 cells

(A) Extracellular oxygen consumption rate (OCR) analysis of light-damaged ARPE19 cells with or without Y-27632 treated.

(B) Quantification of oxygen consumption rate (OCR) in mitochondrial basal respiration, maximal respiration, ATP production, and spare respiratory capacity.

971

Supplemental Figure 5. Analysis of mitochondrial movement and network structure after Y-27632 treatment

(A, B) Miro1 protein levels were detected and quantified in control and Y-27632 groups by Western blotting. n=3, t test, mean±SEM; ns, not significant.

(C) Visual description of terms used in this study.

(D, E) The number and average size of mitochondrial networks in control and Y-27632 groups were quantified. n (control)=88, n (Y-27632) =95. Mann-Whitney test, median ± interquartile range; ns, not significant.

980

981

982   **Movies**

983

984   **Movie 1.** Y-NTs formation and mitochondrial transfer in bright field

985   ARPE19-mito-GFP cells (green) and ARPE19-mito-RFP cells (red, CM, blue) were

986   co-cultured at a 1:1 ratio in direct contact.

987

988   **Movie 2.** Y-NTs formation and mitochondrial transfer with F-actin staining

989   ARPE19-mito-GFP cells (green) and ARPE19-mito-RFP cells (red, CM, blue) were

990   co-cultured at a 1:1 ratio in direct contact, and all cells were stained with phalloidin

991   (magenta).

992

993   **Movie 3.** Mitochondrial movement in ARPE19 cells with Y-27632 treatment

994   ARPE19-mito-GFP cells (green) and ARPE19 cells (CM, blue) were co-cultured at a

995   1:1 ratio in direct contact.

996

997   **Movie 4.** Mitochondrial movement in ARPE19 cells without Y-27632 treatment

998   ARPE19-mito-GFP cells (green) and ARPE19-mito-RFP cells (red, CM, blue) were

999   co-cultured at a 1:1 ratio in direct contact.